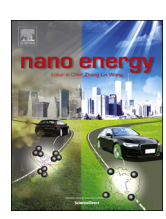
FISEVIER

Contents lists available at ScienceDirect

Nano Energy

journal homepage: www.elsevier.com/locate/nanoen



Full paper

A self-healing layered GeP anode for high-performance Li-ion batteries enabled by low formation energy



Wenwu Li^{a,b}, Xinwei Li^{c,*}, Jiale Yu^a, Jun Liao^a, Bote Zhao^b, Liang Huang^{e,*}, Ali Abdelhafiz^b, Haiyan Zhang^a, Jeng-Han Wang^f, Zaiping Guo^d, Meilin Liu^{b,*}

- ^a School of Materials and Energy, Guangdong University of Technology, Guangzhou, 510006, PR China
- School of Materials Science & Engineering, Georgia Institute of Technology, Atlanta, GA, 30332, USA
- ^c Department of Mechanical and Energy Engineering, Southern University of Science and Technology, Shenzhen, 518071, PR China
- d Institute for Superconducting and Electronic Materials, School of Mechanical, Materials and Mechatronics Engineering, University of Wollongong, North Wollongong, NSW, 2500, Australia
- e The State Key Laboratory of Refractories and Metallurgy, Wuhan University of Science and Technology (WUST), Wuhan, 430081, PR China

ARTICLE INFO

Keywords: Self-healing Layered structure Ge-based Anode Li-ion batteries

ABSTRACT

Ge is considered a promising anode candidate for Li-ion batteries (LIBs); however, its practical applicability is hindered by the relatively slow Li-ion diffusion owing to the stiffness of the diamond-like structure. Inspired by little difference in electronegativity between Ge and P, we have designed a novel layered GeP anode for LIBs, which can be readily synthesized using a mechano-chemical method and a subsequent low-temperature annealing. In particular, GeP demonstrates the best performances among all Ge-based anode materials studied, attributed to its fast Li-ion diffusion compared to Ge counterpart and a unique Li-storage mechanism that involves intercalation, conversion, and alloying, as confirmed by XRD, TEM, XPS, and Raman spectroscopy. Specially, the initial layered crystal structure of GeP can be reconstructed during charging due to its low formation energy, thus offering remarkable reversibility during cycling. Further, this study implies that the formation energy of crystal structures could be an important parameter for strategic design of large-capacity anode materials for LIBs.

1. Introduction

Although Ge has comparable volumetric capacity to that of silicon, its application is still hindered by its relatively low Li-ion, electron transportation capability and large volume expansion during cycling for rechargeable lithium-ion batteries (LIBs) due to the inherent stiffness of its diamond-like crystal structure. To overcome these problems, a number of Li-inert transition metals (like Fe) and Li-reactive compounds (like oxides, and sulfides) have been extensively studied [1]. Unfortunately, the former severely reduces energy density and the latter has been proven to only contribute to capacity above a potential of 1.1 V, inappropriate for anodes. Moreover, oxygen and sulfur have poor energy efficiency in full cells caused by low initial coulombic efficiency and large polarization losses due to the large formation energy of Li₂O, and the dissolution of the electrochemical intermediate Li₂S into conventional electrolytes. In addition, other strategies have also been applied to optimize Ge-based materials, such as the application of

a thin carbon coating, reducing the particle-size, forming micro/mesoporous structures, and preparing self-standing thin-films or hierarchical nanowire/nanotube arrays [2,3]. Unfortunately, these approaches often require complicated synthetic procedures and/or high fabrication costs which prevent their commercialization even though the as-designed nanomaterials exhibit enhanced Li-storage performances in some aspects, compared to pure Ge electrodes.

Considering the weaker electronegativity of P than that of O and S, black P has been used as an anode material for rechargeable metal ion batteries; it has delivered excellent electrochemical energy-storage performances attributed to its fast transport capability of the Li-ion and electron endowed by the layered structure. However, it still has a long way to go due to difficulty in heat-management resulting from its spontaneous degradation into red P above $125\,^{\circ}\mathrm{C}$ [4,5]. To ensure safety, more attention has been devoted to binary phosphides [6–13], especially for Fe/Sn-P series. Unfortunately, most of them usually suffered from serious capacity decay and low initial coulombic efficiency

E-mail addresses: lixw@sustc.edu.cn (X. Li), huangliang1986@wust.edu.cn (L. Huang), meilin.liu@mse.gatech.edu (M. Liu).

f Department of Chemistry, National Taiwan Normal University, Taipei, 11677, Taiwan

^{*} Corresponding authors.

due to their electrode structure destruction especially for their initial crystal structures [6–9,13]. During the lithiation of these conversion-based anode materials, the initial crystal structures were broken and difficult to be reconstructed even after Li-ion release. The resulting electrodes degraded into the mixture of the metal and phosphorus other than original phosphides with structural advantages after the initial cycle. Their cycle stability was only marginally extended via the elevated cut off potential to alleviate the structural degradation at the expense of the valuable capacity. Therefore, searching for a novel phosphide, which enables self-healing during cycling to ensure long operational life without sacrificing capacity and finding out the fundamental reason behind this at the atomic level are still of great scientific importance and practical value.

In view of the above-mentioned facts and the small difference in electronegativity between Ge and P, here we propose to introduce 30 wt.% cheap P into Ge to develop a novel layered Ge-based anode material for LIBs via facile ball milling, along with a low-temperature annealing, expecting Li-storage merits and synergistic effect brought by P. The characterization techniques and first-principle calculations covalidate the as-synthesized Ge-based electrode obtained superior Listorage reaction kinetics to Ge. Furthermore, an interesting Li-storage mechanism that involves intercalation, conversion with alloy is co-validated using XRD, HRTEM, selected area electron diffraction (SAED), X-ray photoelectron spectroscopy (XPS), Raman spectroscopy, and electrochemical measurements. Surprisingly, we find that the as-synthesized GeP anode has an outstanding self-healing ability in terms of re-constructing its original layered crystal structure during charging, due largely to its low formation energy, according to the first-principle calculations. This special healed phenomenon helps regain layered Listorage merits and alleviates electrode structural degradation, thus enabling GeP/C composite with the best performances among Ge-based anodes studied, in terms of cyclability, energy efficiency, and reaction kinetics.

2. Experimental and calculation section

2.1. Material synthesis

The GeP sample was synthesized via a facile mechanical milling (Fritsch Pulverisette-6) by sealed Ge and amorphous red P powders in a given molar ratio of 1:1 into a steel vessel (Volume: 500 ml) filled with Argon, using a milled speed of 350 rpm. (2.0 h), together with a subsequent calcination at 370 °C for 0.5 h under argon to enhance its layered crystallinity (heating rate of 2 °C/min). The milling balls are steel balls with the radius of 1.0 cm, and the ball to material weight ratio is 20:1. Each run contains 5g powder. The GeP/C composite was prepared in a similar manner by a second milling of the lab-prepared GeP and commercial graphite (mass ratio is 7:2) under the speed of 350 rpm. for 1.0 h. Similarly, the corresponding anode materials utilized for comparisons such as milled Ge, milled P, Ge/C and P/C are ball milled at the same experimental conditions.

2.2. Material characterization

The as-synthesized phases were characterized via X-ray diffraction (PANalytical X'pert PRO-DY2198 with Cu-K α radiation). The morphologies and micro-structures of the above-synthesized products were observed by field-emission scanning electron microscope (FEI Quanta650), transmission electron microscope (JEOL JEM 2100). The valence and composition analysis of GeP, its carbon composite and corresponding discharge/charge products were also performed by X-ray photoelectron spectroscopy (Thermo Fisher ESCALab250 with the monochromatic 150 W Al K α radiation), and confocal Raman spectrometer (Raman, WTEC ALPHA300 with the 532 nm excitation laser).

2.3. Electrochemical characterization

For pure phase GeP, Ge + P mixture, milled Ge and milled P electrodes, the active materials were blended with carbon black as well as binder of lithium polyacrylic acid (Li-PAA) in 7:2:1 (mass ratio). The slurry was pasted on the copper foil and then dried at 90 °C in vacuum. overnight. For GeP/C, Ge/C and P/C electrodes, the active materials were directly blended with the binder in 9:1 (weight ratio) without any conductive agent. Loading active material is about 1.5-2.0 mg cm⁻². The electrolyte is $LiPF_6$ (1.0 mol L^{-1}) dissolved in the mixed solvents of dimethyl carbonate, ethyl methyl carbonate and ethylene carbonate in a volume ratio of 1:1:1. The coin-typed cells (CR2032) were assembled in the glovebox (Mbraun, Labmaster 130) with the H₂O and O₂ concentrations below 0.01 ppm. The Li metal was used as counter and reference electrodes. The Li-storage discharge/charge tests were carried out on the testing system (Hokuto Denko, HJ1001SD8) and the cyclic voltammetric tests were carried out on the electrochemical workstation (Autolab, Pgstat 302N).

2.4. Calculations details

All DFT calculations were performed by CASTEP, with the generalized gradient approximation (GGA) and Perdew-Burke-Ernzerhof (PBE) exchange correlation function. The ultrasoft pseudopotential was used to describe electron-ion interaction and a plane-wave basis set with a cut off energy of fine quality (544.2 eV) was applied to represent the valence orbitals. The convergence criteria were set to a fine quality. Electronic energies were calculated with a self-consistent-field (SCF) tolerance of $1.0 \times 10^{-6} \, \text{eV}$ atom⁻¹. Structural optimizations were performed until the energy and force of the system converged to within $1.0 \times 10^{-5} \,\text{eV}$ atom⁻¹ and $3.0 \times 10^{-2} \,\text{eV}\,\text{Å}^{-1}$, respectively. The Brillouin zone integration was sampled by Monkhorst-Pack k-point mesh with grid spacing of $7 \times 10^{-2} \,\mathrm{A}^{-1}$. The transition-state structure was obtained using by the complete LST/QST method to calculate the minimum-energy profile along the prescribed Li diffusion pathways, with the tolerance for all root-mean-square forces on an atom of $5 \times 10^{-2} \, \text{eV} \, \text{Å}^{-1}$. For the calculation of band structure and density of states (DOS), the first Brillouin zone was sampled with grid spacing of $3 \times 10^{-2} \,\mathrm{A}^{-1}$ on the basis of Monkhorst-Pack special k-point scheme. To calculate the formation energy, the following equation was used:

$$E_f = E_{MP}$$
 - μ_M - μ_P

where E_{MP} is the energy of MP in one unit cell, μ_M is the related chemical potential of Ge atom (space group FD-3M) or Fe (space group IM-3M) atom. The μ_P is the related chemical potential of P (space group CMCA) atom.

3. Results and discussion

3.1. Preparation and characterization of layered GeP

Among Group IVA-VA compounds, Ge and P could crystallize into an interesting monoclinic phase in the formula of GeP under extreme experimental conditions like high-temperature and high-pressure in 1970s [14]. As shown in Fig. S1a, its crystal structure has an open layered framework with interlayer spacing of $\sim 6.3\,\text{Å}$, large enough for Li-ion transport and storage (the radius of Li ion is only 0.73 Å). Specifically, as shown in Fig. S1b-Fig. S1c, within each layer, Ge-Ge pairs are surrounded by six P atoms forming a distorted trigonal antiprism, while each P atom is coordinated by three Ge atoms and the layers stack through lone-pair interaction between the P atoms that are confined within the adjacent two layers. Considering existing covalent Ge-Ge, and Ge-P bonds within the layered structure, the formation energy of GeP must be low, which would favor reconstruction of its initial crystal structure upon its de-lithiation process when served as an anode for LIBs. As shown in Fig. 1a, the interesting GeP phase have been

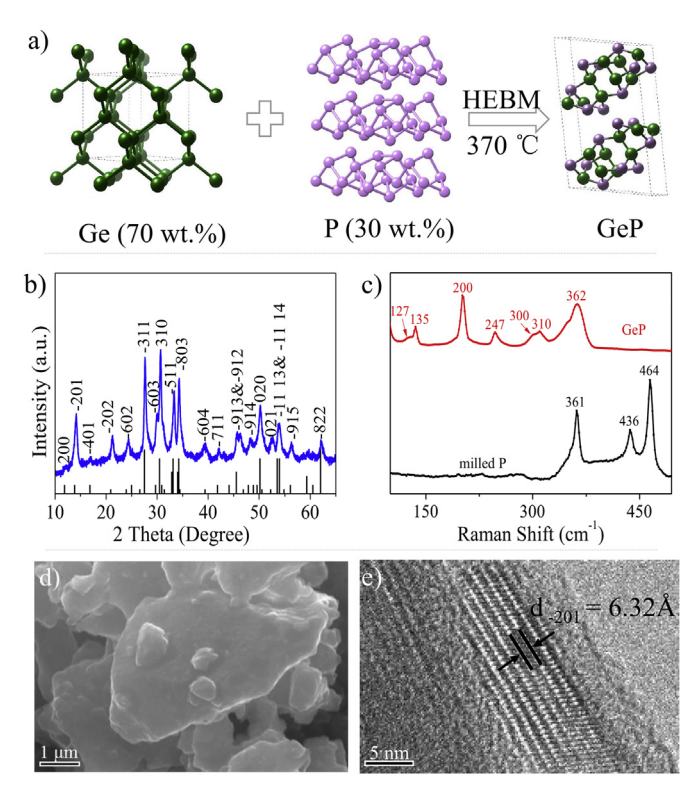


Fig. 1. a) the synthesis procedure of layered monoclinic phase GeP; b) XRD pattern of the as-synthesized sample; c) the Raman spectra of the as-synthesized sample with that of milled P for comparison; d) the high-magnitude field-emission scanning electron image of layered GeP phase; e) the high-resolution transmission electron image of layered GeP phase. Note that HEBM means high-energy mechanical ball milling.

synthesized originally by high-energy mechanical ball milling the mixture of P and Ge powders in the molar ratio of 1: 1, together with subsequent low-temperature calcination at 370 °C. Fig. 1b presents the XRD pattern of the as-prepared GeP phase, which corresponds to the monoclinic phase GeP, much different from the raw material of Ge, P, as well as the mixture as shown in Fig. S2. Moreover, we carried out XRD analysis of the precursor before annealing (Fig. S3). Clearly, the layered structure of GeP has not vet been formed before annealing: thus, the annealing is a necessary step to obtain the desired phase. To further validate its successful preparation, we conducted the Raman Spectroscopy. As exhibited in Fig. 1c, the Raman signals of the assynthesized GeP differ from that of the milled P at the same experimental conditions, while well-consistent with that of the single crystal of monoclinic phase GeP prepared by high-temperature chemical vapor transportation, suggesting that this novel phase have formed [15]. The computed vibrational modes (as shown in Fig. S4), consistent with the experimental Raman spectrum of GeP, revealed that the two intense peaks at 362 and 200 cm^{-1} (computed as 362/352 and 203/200 cm^{-1} , respectively) are assigned for P-Ge and Ge-Ge stretching modes, respectively. The other three observable peaks in the region of 300-310, 247, and 135 cm⁻¹ (computed as 320/324, 252/244 and 131 cm⁻¹ respectively) correspond to the Ge-P-Ge skeleton stretching, rocking, and plane deformation, respectively. The Raman spectrum of as-synthesized GeP is notably different from that of the as-milled P, where the three observable peaks are centered at 464, 436 and 361 ${\rm cm}^{-1}$ (the P-P stretching modes, Fig. S5), confirming that the synthesized GeP sample is not a physical mixture of Ge and P (Fig. S6). To observe its morphology and micro-structure, the field-emission scanning electron microscope (FESEM) and low-magnitude TEM have been performed, as shown in Fig. 1d and Fig. S7, the as-prepared secondary GeP aggregates obtain large bumpy shapes with particle size up to several micrometers.

More detailed microstructure probed by the HRTEM image (Fig. S8) indicates the d-spacings of 0.324 nm and 0.301 nm, which corresponds to the crystal planes of (-311) and (-603), respectively. Its clear ring-like selected area electron diffraction pattern (inset in Fig. S8), well-consistent with corresponding XRD crystal plane indexes without any other superstructure, further validates that its pure phase and existence in the form of small nanocrystals with their sizes of 20–50 nm based on the Scherrer equation ($d = 0.9\lambda/\beta\cos\theta$) calculation, low-magnitude dark-field TEM (Fig. S9), and HRTEM observation. Moreover, the layered crystal structure of GeP can be directly observed. As shown in Fig. 1e, the d-spacing (Fig. S1a) of \sim 0.63 nm can be well-observed, corresponding to the crystalline plane of (-201).

3.2. Li-storage behaviour superiority of layered GeP

Inspired by advantageous structural and compositional features, specifically binary Li-reactive components, layered structure and small differences in electronegativity between its two constituents, we anticipated that GeP anode would exhibit excellent Li-storage performances with unique electrochemical behavioural characterizations. To prove this point, we compared the first-cycle electrochemical Li-storage behaviors of GeP with that of Ge and P mixture electrode (a mixture with milled Ge and milled P in a molar ratio of 1:1, denoted as Ge + P). And their initial-cycle galvanostatic discharge/charge profiles were plotted together, as presented in Fig. 2a, at a current density of 100 mA g⁻¹, over potential window of 0.005–3.0 V. As seen clearly, this novel layered GeP delivers an initial coulombic efficiency up to 93%, surpassing that of most reported Ge-based anodes and even comparable to that of commercial graphite. While the Ge + P mixture electrode only delivered 79%, compromising that of milled Ge (86.5%) and milled P (26.5%) electrodes, as shown in Fig. S10. Moreover, the discharge/charge profiles of GeP appear to be much smoother with a smaller over-potential, compared with that of Ge + P mixed electrode. These special electrochemical phenomena accord well with the initial current-potential curves (CVs) of the as-prepared GeP and Ge + P mixture electrodes shown in Fig. 2b. All these electrochemical behaviours exhibited by the layered GeP electrode would be propitious to high energy efficiency, when served in full cells. From Fig. 2c, we can see that GeP anode could deliver a large reversible capacity of 1800 mA h g⁻¹, cycling over 60 cycles without decay, longer cycle-life than the Ge + P mixture, or milled Ge electrodes prepared by the same experimental conditions. The larger reversible capacity and better cycle stability of GeP than that of Ge mainly derived from the introduction of P and smaller volume expansion. Specifically, as calculated in Table S1, the volume expansion of GeP is only 330%, smaller than that of Ge, 370%, based on final discharge products, respectively. Also seen from Fig. 2d, even at an aggressive current density of 5 A g⁻¹, the layered GeP can still deliver ca. $800 \, \text{mA} \, \text{h} \, \text{g}^{-1}$, approaching 46% initial capacity retention at a current density of 100 mA g^{-1} , much better than the Ge + P mixture (24%), and milled Ge (25%) electrodes. The superior Li-storage rate performances of GeP mainly benefit from its faster transfer of the Li-ion and electron endowed by inherent structural superiority as discussed below.

3.3. Li-ion, electron transportation calculation of layered GeP

To obtain more insightful understanding of Li-ion mobility and migration pathways within the interlayers of GeP, a new Li-storage anode material without similar structural characteristics reported before, atomic-scale simulations into local structure and Li-ion transport properties are of vital importance. Therefore, we evaluated Li-ion diffusion energy barriers for various possible Li-ion transport mechanisms at the atomic level based on density function theory (DFT). The theoretical XRD pattern corresponding to the as-simulated model is well consistent with the experimental results shown in Fig. S11, which indicated the rationality of the simulation. Fig. 3a and Fig. S12 presented

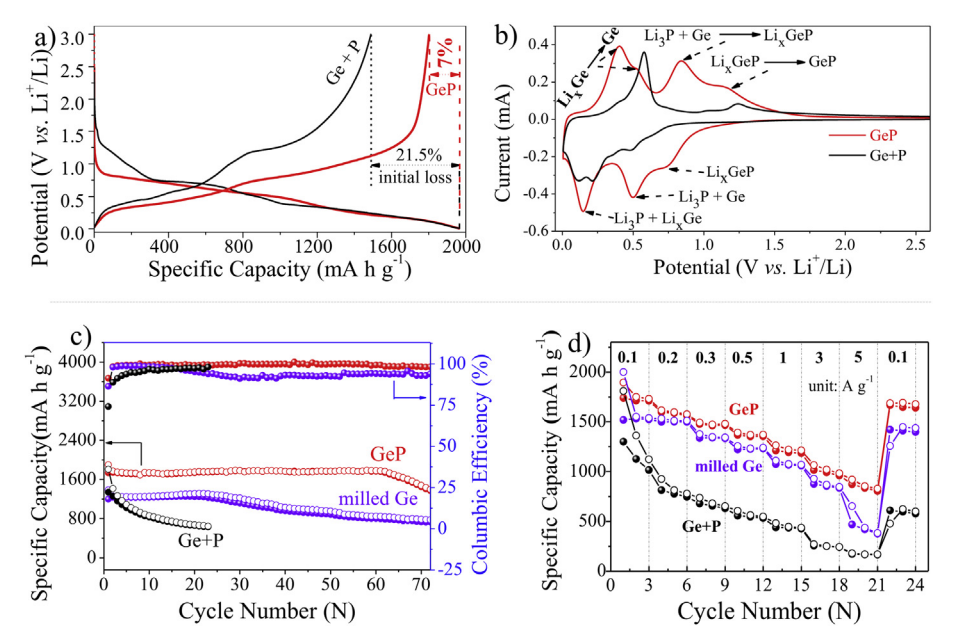


Fig. 2. a) the potential-specific capacity curve of the as-synthesized GeP anode at the first cycle, with that of Ge $\,+\,$ P mixture electrode for comparison; b) the first cyclic voltammetric curve (CV) contrast between GeP and Ge $\,+\,$ P mixture; c) the specific capacity and coulombic efficiency-cycle number curve of GeP anode with that of Ge $\,+\,$ P mixture and single-component Ge electrodes for comparison; d) the reversible capacity-current density curve of GeP with that of Ge $\,+\,$ P mixture and single-component Ge electrodes for comparisons.

the energy profiles mapped out by calculating the Li-ion diffusion energy barrier along the [010], [102], and Z-axis diffusion paths within the crystal structure of GeP, respectively. As seen clearly, it is much easier for Li-ion transport along the [010] direction, where the energy barrier is only 0.34 eV, less than that of Ge (0.66 eV, as shown in Fig. 3b). These simulation results prove that Li-ion diffusion rate is faster within the interlayers of GeP, profiting from its lower migration energies, which helps rationalize the observed superiority in Li-storage behaviors like excellent rate capability, fast reaction kinetics and small polarization to its single-component or Ge + P mixture electrodes. More interestingly, as shown band structure in Fig. 3c, we find that Liion intercalation into the interlayers of GeP excites the metallic band structure featured by no band gap from initial semiconductor of GeP with a band gap of 0.426 eV (Fig. 3d). Also, the superior metallic conductivity of LixGeP to that of the initial GeP can also be clearly seen from their density of state (DOS) profiles mapped out in Fig. S13. The total DOS value of the intermediate Li_x GeP at Fermi Level is calculated to not be zero, and also much larger than that of initial GeP, further confirming the metallic conductivity of the intermediate LixGeP. The simulated models of Li_xGeP used for the calculation were shown in Fig. S14. Accompanied with increasing Li-ion intercalation amount into the interlayers of bulk GeP, the extra electrons were also inserted into the conduction band, which could improve the electron transfer capability substantially [16]. To validate the enhanced electronic conductivity, we performed electrochemical impedance spectra measurements of GeP and Ge electrodes. As shown in Fig. S15, the charge transfer resistance (Rct = 31 Ω) of GeP electrode is much smaller than that (65 Ω) of Ge. Moreover, the Li-ion diffusion coefficient of GeP is ca. one order of magnitude larger than that of Ge [17]. The dramatically improved electronic conductivity excited by the Li-ion intercalation presented the structural superiority of layered GeP, which would further enhance its prominent Li-storage performances.

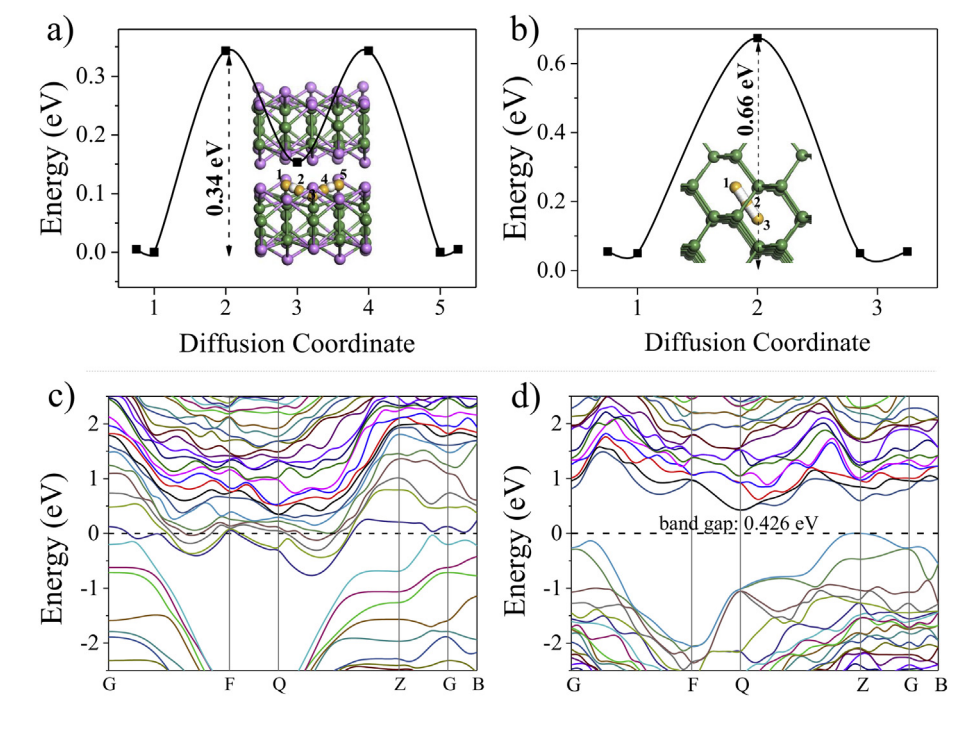


Fig. 3. a) the calculated energy barrier-diffusion coordinate profile of GeP and the inserted schematic illustration is the corresponding diffusion pathways of Li atoms within the GeP interlayers along the [010] direction; b) the calculated energy barrier-diffusion coordinate profile of Ge and the inserted schematic illustration is the corresponding diffusion pathways of Li atoms. c) the electronic structure of lithiated layered GeP phase (Li_xGeP); d) the electronic structure of original layered GeP phase.

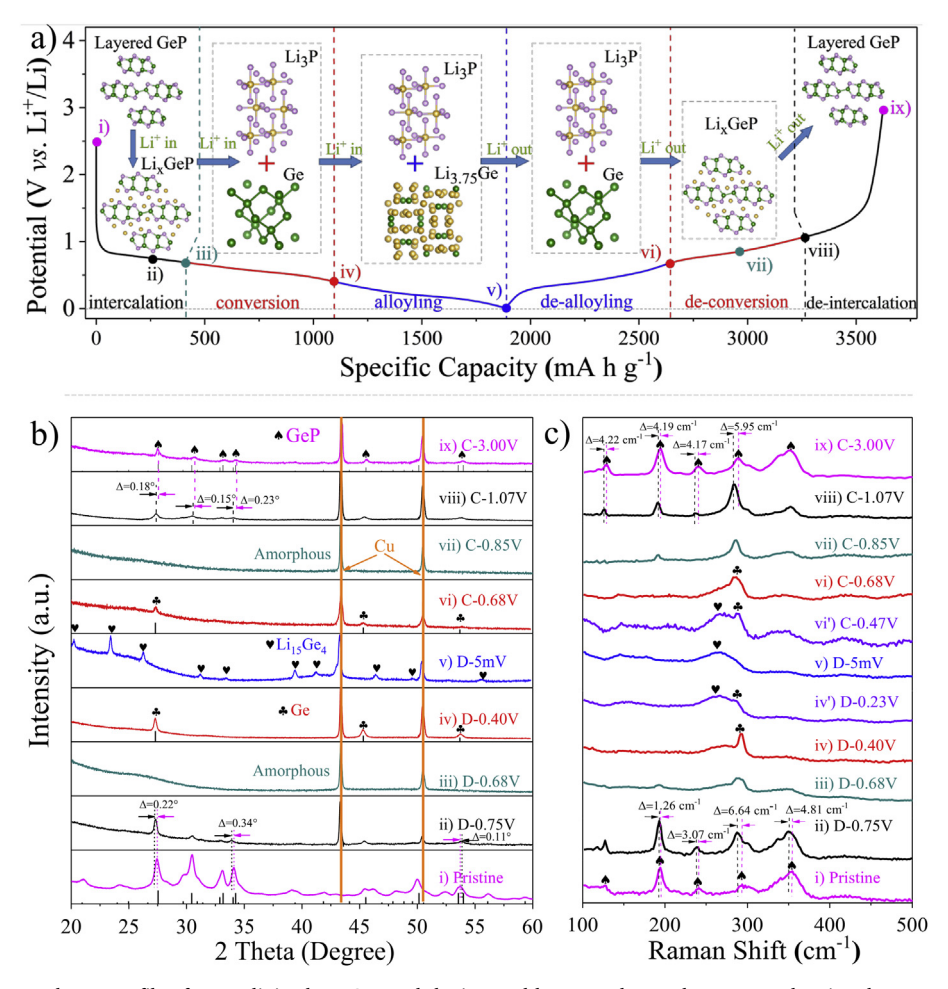


Fig. 4. a) the initial discharge/charge profile of monoclinic phase GeP and the inserted letters and crystal structures showing the corresponding discharge/charge states and phase-evolution processes, respectively; b) XRD patterns collected at various selected potential states accompanied by the initial lithiation/de-lithiation process; c) Raman spectra captured during the initial discharge/charge process. Both XRD and Raman results prove the high reversibility of layered crystal structure of monoclinic phase GeP electrode.

3.4. Li-storage mechanism investigation of layered GeP

To observe the structural evolution of the as-synthesized microsized GeP anode accompanied by lithiation/delithiation process, we further conducted various characterization techniques including XRD, TEM, XPS, and Raman Spectroscopy. From the XRD patterns (Fig. 4b) collected at various potential points as indicated in the discharge/charge profiles (Fig. 4a) operated at a current rate of 100 mA g⁻¹ within the potential window of 0.005-3.0 V, we can see that in stage I (from the open circuit potential to 0.68 V, lithiation), with increasing Li-ion intercalated into the GeP electrode, the initial fingerprint peak positions of (-311), (310), (-511), (-803), (-913) begin to shift towards the lower 2 theta angle and simultaneously their peak intensities begin to diminish, as shown in Fig. 4b-ii. These shifted peak positions and reduced intensities can be attributed to the lattice expansion of the assynthesized microsized GeP incurred by the Li-ion intercalation into the interlayers of GeP to form into LixGeP. Note that each deviation of these peaks is different, to some degree, as exhibited in Table S2, which can be ascribed to anisotropic expansion due to various Li-ion diffusion capability along different directions as calculated above (Fig. 3a and Fig. S12) [18]. The visualizations of expanded crystal plane distances of (-311), (310) further validate the Li-ion intercalation into the interlayers of GeP, compared with that of initial GeP, as shown HRTEM by Fig. 5a-ii. Subsequently, as shown in Fig. 4b-iii and Fig. 5a-iii, we can detect the amorphous state of LixGeP, corresponded to the discharge capacity of 400 mA h g⁻¹, and thus the x value can be evaluated to be

one, namely LiGeP. Stage II: on further lithiation, from the corresponding XRD pattern shown by Fig. 4b-iv, we can observe typical fingerprint peaks of Ge, namely, (111), (220), and (311), which indicate the intermediate product LixGeP has decomposed. Also, the decomposition can also be validated by the HRTEM results shown in Fig. 5aiv. The typical crystal plane d-spacings of 0.326 nm, and 0.20 nm corresponding to crystal plane of (111) and (220) of the separated Ge, respectively, as well as 0.19 nm and 0.33 nm corresponding to (004) and (101) of the produced Li₃P, can be observed, which further proved the electrochemical intermediate product LixGeP degraded into the mixture of Ge and Li₃P. Note that no observation of Li₃P phase in the XRD pattern can be ascribed to the low P content within GeP or low crystallinity caused by lithiation. Stage III: when the anode was fully discharged to the state of 0.005 V, as shown in Fig. 4b-v, the new diffraction pattern can be identified to be Li_xGe (x = 3.75, PDF card NO. 89-2584), indicating the separated Ge during the conversion reaction continues to contribute to the larger capacity. The further lithiation of Ge can also be confirmed by detecting LixGe signals in the HRTEM shown in Fig. 5a-v. Stage IV: upon charging to 0.68 V, the LixGe fingerprint peaks disappeared while Ge peaks emerged (Fig. 4bvi), indicating that Li-ions were first extracted from the Li_xGe alloys. The results can also be validated by HRTEM results shown in Fig. 5a-vi. Stage V: as the de-lithiation potential increased to 0.85 V, the characteristic signals of the Li₃P have vanished with regard to HRTEM shown by Fig. 5a-vii. This indicates the Li-ions were further extracted from Li₃P and subsequently the electrode became amorphous (Fig. 4b-

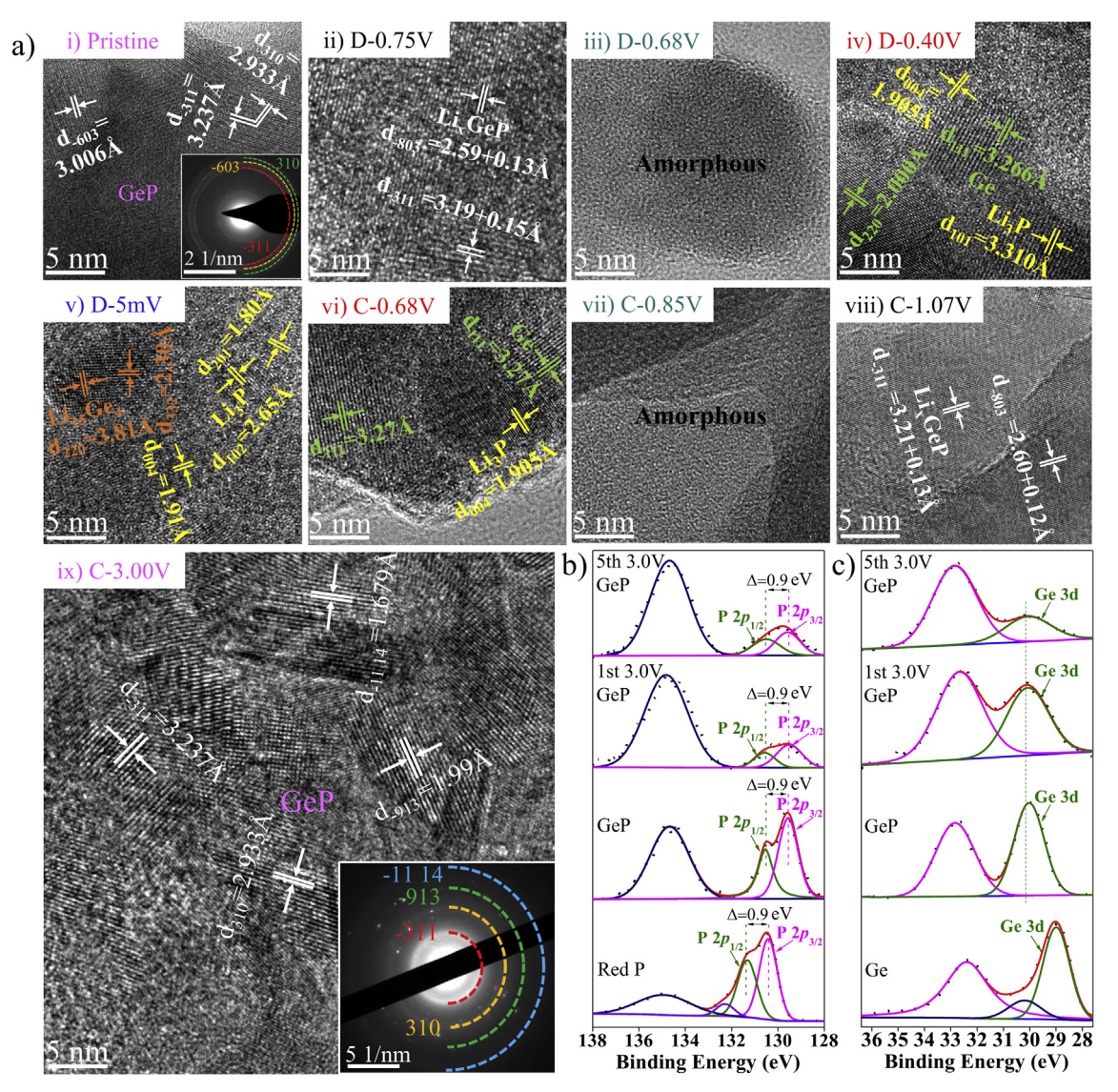


Fig. 5. a) the ex-situ HRTEM images along with SAED and the selected potentials as marked in Fig. 4a; b), c) the ex-situ XPS data of the as-synthesized GeP anode and their contrasts with the raw material of red P and Ge. The similarity after cycling indicate the as-synthesized GeP anode is highly reversible.

vii). The amorphous transformation indicated the electrode experienced the structural readjustment to form LixGeP intermediate as shown by Fig. 4b-viii and Fig. 5a-viii, due to the self-healing ability endowed by this special structure. The phenomenon has also been observed in transition metal chalcogenides before [19]. Stage VI: with further Li-ion extracted from the Li_{x}GeP intermediates, surprisingly, the characteristics of the as-synthesized GeP have re-appeared again in terms of XRD (Fig. 4b-ix), HRTEM (Fig. 5a-ix) and XPS (Fig. 5b-c, discharge/charge profiles shown in Fig. S16), implying its original crystal structure has been re-constructed with increased potential driving force during charging. Besides the evidences from XRD and TEM based on crystallography together with XPS, we further performed Raman to confirm whether the above-mentioned Li-storage mechanism exists. As shown in Fig. 4c-ii, we can see that all the Raman characteristic bands of the layered GeP just shifted to a lower wavenumber and the corresponding intensities became weaker until it almost disappeared, which corresponds to discharge depth to ca. 400 mA h g⁻¹ corresponding to stage I above. The deviating phenomenon in the Raman spectra can be assigned to the delicate change in the stretching/ bending modes of Ge-P and Ge-Ge bonds by the reason of structural topotactic transition of GeP corresponding to Li_xGeP. Therefore, the transition resulted from increasing Li-ion intercalation amount into the

interlayers of GeP to form Li_xGeP (x < 1.0). In the subsequent discharge stage (Fig. 4c-iii), the Raman fingerprint peak of the separated Ge appears at the wavenumber of 299 cm⁻¹, which indicates that the Li-ion intercalation compound LixGeP began to decompose into Ge, corresponding to conversion reaction. With increased Li-ion uptake amount, the inherent signal of the separated Ge became stronger until the discharge capacity reached ca. 800 mA h g⁻¹, where the Li_xP was completely lithiated into Li₃P. No observation of Raman characteristic signals of the Li_xP can be attributed to the low P content within GeP. As discharge continues (Fig. 4c-iv), the fingerprint peaks of the separated Ge began to shift and became weaker until the peaks disappeared at the end of discharge. By contrast, the characteristic peaks of Li_xGe became stronger (Fig. 4c-v) as the result of further lithiation of separated Ge. More surprisingly, when charged, all the processes (from Fig. 4c-vi to Fig. 4c-ix) are highly reversible until the re-appearance of characteristic peaks of GeP, which suggests the local structure of GeP has been reconstructed. Therefore, the Raman results accord well with the conclusion of crystallography and XPS, and this further confirms the rationalization of Li-storage mechanism proposed above for the as-synthesized GeP. Furthermore, in terms of electrochemical behaviors, from the initial 20-cycle CV curves of monoclinic GeP as shown in Fig. 2b and Fig. S17, we can clearly see the corresponding six-stage mechanism

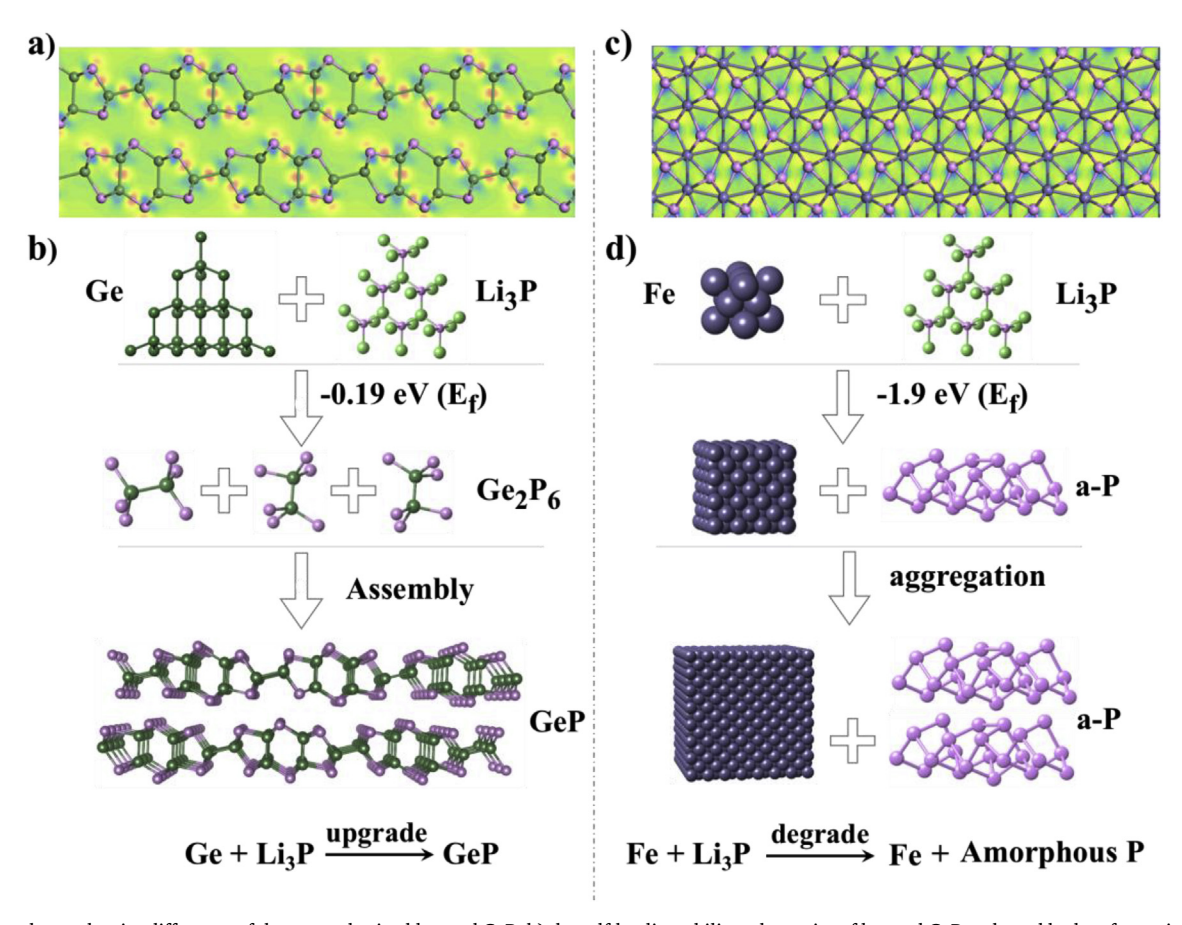


Fig. 6. a) The charge density difference of the as-synthesized layered GeP; b) the self-healing-ability schematics of layered GeP endowed by low formation energy (E_f: -0.19 eV) during charging; c) the charge density difference of the non-layered FeP phase; d) the degradation schematics of FeP caused by large formation energy (E_f: -1.9 eV) during charging.

process. For the initial CV curve, during the reduction, there exists a broad shoulder in the potential range from 1.25 to 0.66 V, which implies the Li-ion intercalation into the interlayers of GeP to form Li_xGeP and little solid electrolyte interface formation due to low specific surface area because of ball milling together with calcination. With potential reduced to 0.4 V, the formed electrochemical intermediate product Li_xGeP began to decompose into Li₃P and Ge [20]. As the cell is further scanned to 0.06 V, another reduction peak appears, which means that the separated Ge is further lithiated into Li_xGe (x < 3.75). When reversely scanned to the positive potential of 0.41 and 0.53 V, there appears two oxidation peaks, which corresponds to Li-ion extraction from Li_xGe (x < 3.75); as potential is further increased to 0.85 V, the Li-ions would be extracted from Li₃P and meanwhile the electrode probably starts to form into the intermediate electrochemical product Li_xGeP [21,22]. At the peak centred at 1.15 V, Li_xGeP experienced the de-lithiation process. Finally, the initial monoclinic phase GeP has re-formed again when arrived at the cut-off potential of 3.0 V. Evidently, the CV profiles (Fig. S17) remain almost the same from the second cycle onward, implying a highly reversible six-stage electrochemical Li-storage process and a well-re-constructed crystal structure of the as-synthesized microsized GeP. The discharge/charge curves basically show continuous trend instead of any significant plateaus or potential changes when transitioning from one Li storage stage to another. This is originated from the relatively overlapped redox potentials for Li-storage in Ge and P.

To recap, the proposed six-stage Li-storage mechanism of the assynthesized microsized GeP are: (i) the intercalation reaction (GeP \rightarrow Li_xGeP, 2.5–0.68 V); (ii) conversion reaction (Li_xGeP \rightarrow Ge + Li₃P, 0.68–0.40 V); and (iii) alloy reaction (Ge \rightarrow Li_yGe, 0.40–0.005 V). Conversely, (iv) de-alloying reaction (Li_yGe \rightarrow Ge, 0.005 \rightarrow 0.68 V); (v)

de-conversion reaction (Ge + Li $_3$ P \rightarrow Li $_x$ GeP + (3-x) Li $^+$ + (3-x) e $^-$, 0.68 V \rightarrow 1.07 V); and (vi) de-intercalation of Li $_x$ GeP to form GeP crystal phase (Li $_x$ GeP \rightarrow GeP + x Li $^+$ + x e $^-$, 1.07 V \rightarrow 3.0 V). Also, the reversed de-alloy, de-conversion and de-intercalation processes appear to be reversible, giving rise to the high initial coulombic efficiency up to 93%, while the little irreversible capacity loss mainly arises from SEI formation in the initial cycle. Considering the XRD, TEM, XPS, and Raman results along with the electrochemical Li-storage behavioural characteristics, Li-storage mechanism of the as-synthesized microsized GeP can be characterized by combined intercalation, conversion with alloy reactions as follows:

Intercalation stage:

$$GeP + x Li^{+} + x e^{-} \rightarrow Li_{x}GeP (> 0.68 V)$$
 (i)

Conversion stage:

$$\text{Li}_{x}\text{GeP} + (3-x) \text{Li}^{+} + (3-x) \text{e}^{-} \rightarrow \text{Li}_{3}\text{P} + \text{Ge} (> 0.40 \text{ V})$$
 (ii)

Alloy stage:

$$Ge + y Li^{+} + y e^{-} \rightarrow Li_{y}Ge (> 0.05 V)$$
 (iii)

The reverse reactions (iv-vi) occur during the charge process. De-alloy stage:

$$\text{Li}_{v}\text{Ge} \rightarrow \text{Ge} + \text{y Li}^{+} + \text{y e}^{-} (< 0.68\text{V})$$
 (iv)

De-conversion stage:

$$\text{Li}_{3}\text{P} + \text{Ge} \rightarrow \text{Li}_{x}\text{GeP} + (3-x) \text{Li}^{+} + (3-x) \text{e}^{-} (< 1.07 \text{ V})$$
 (v)

De-intercalation stage:

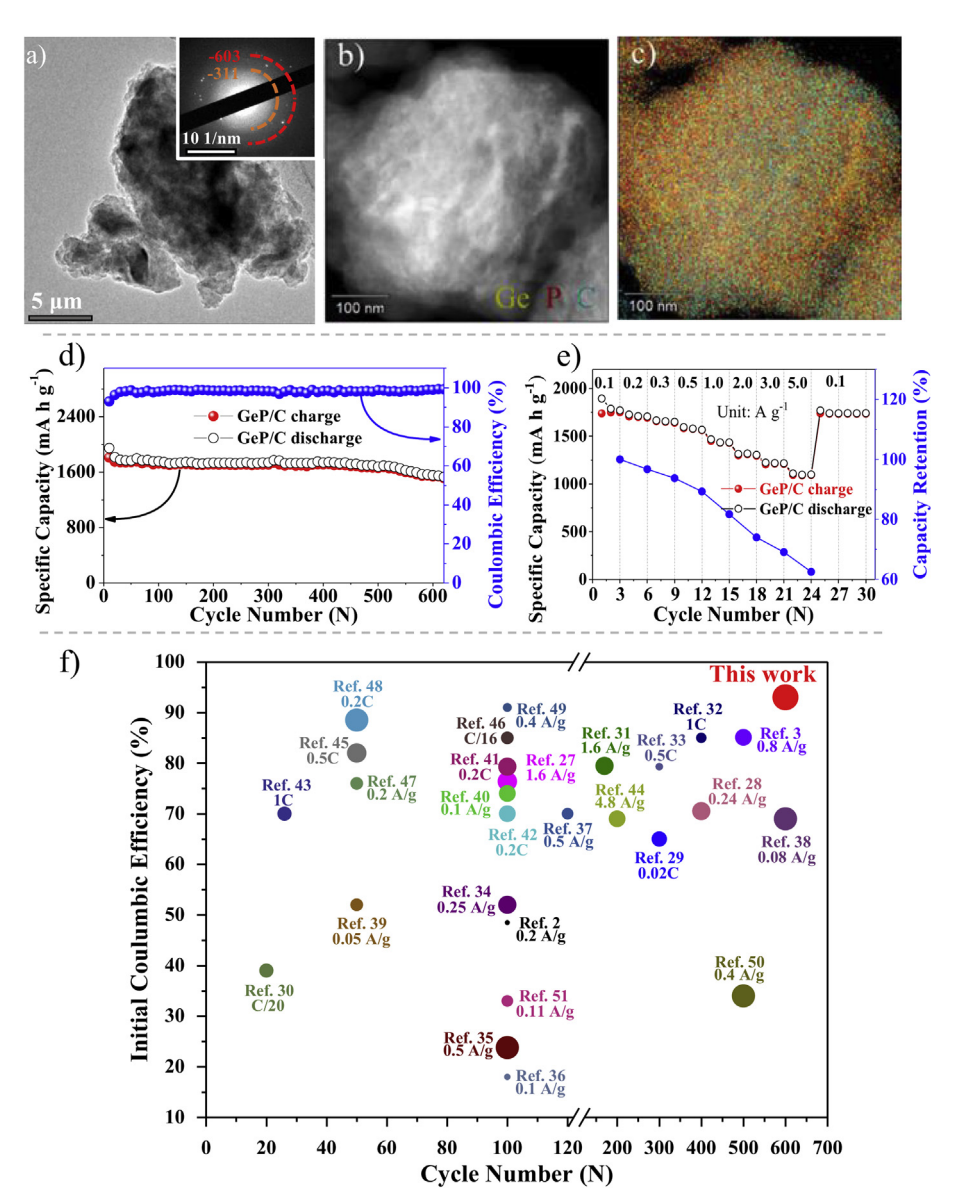


Fig. 7. GeP/C nanocomposite characterization: a) the low-magnitude transmission electron image (TEM) and its corresponding selected area electron diffraction (SAED, inset); b) the frame used for elemental mapping; c) Ge, P, and C integrated elemental mapping image from STEM mode; d) the long cycle-life of the as-prepared GeP/C composite; e) the high-rate performance of the GeP/C composite. f) the performance comparison with all reported high-performance Ge-based anodes in terms of initial coulombic efficiency, reversible capacity and cycle stability at relatively small current density, note that the area of circle denotes the reversible capacity retention at the given cycles.

$$\text{Li}_{x}\text{GeP} \rightarrow \text{GeP} + x \text{Li}^{+} + x \text{ e}^{-} (< 3.0 \text{ V})$$
 (vi)

3.5. The formation energy-structural reversibility relationship

To further explore underlying mechanism behind the structural selfhealing-ability of GeP at the atomic level, DFT calculation was further performed in the viewpoint of formation energy, which can be utilized to evaluate the difficulty of chemical bond cleavage or re-construction [17]. As known, traditional established Li-inert transition metal oxides, sulfides, and phosphides anodes, usually suffer from large initial capacity loss, polarization and little chemical bonding reversibility during their Li-storage processes. Having little chemical bonding reversibility means that their initial crystal structures were disabled to re-construct and the electrode would degrade into a mixture of their corresponding constituent elements rather than forming back into their initial compounds [6-9,23-25]. On the other hand, to our surprise, this newly found GeP, without a similar crystal structure reported as anodes before, has been validated to experience a special self-healing crystal structure process driven by the high potential during charging. However, the underlying mechanism behind this unusual phenomenon still lacks fundamental insights at the atomistic level. Herein, we take GeP and FeP as an example to investigate endopathic factors in the

formation energy based on DFT calculation. The charge density differences in the schematics of GeP phase and FeP phase are exhibited in Fig. 6a and Fig. 6c, respectively. We can see clearly that most electrons (red region) of GeP are located at the middle of Ge-Ge or Ge-P bonds, compared with that of the FeP phase. This demonstrates that the GeP phase has lower polarity, weaker interactions, and lower bonding energy within its crystal structure, compared with FeP. Therefore, it is reasonable that Ge-P bonds could be re-constructed by the increased potential driving force during the charge while FeP does not. Specifically, formation energy of GeP (Fig. 6b) was calculated to be -0.19 eV, ten times smaller than that of FeP ($-1.9\,\mathrm{eV}$ as presented in Fig. 6d), based on formation energy equation: $E_f = E_{MP}$ - μ_M - μ_P , where E_{MP} is the overall ground state energy of MP, μ_M is related chemical potential of Ge or Fe atom, and μ_P is related chemical potential of P atom. For GeP electrode, the small formation energy of Ge-Ge and Ge-P bonds would favor their re-construction and further heal the local structure of GeP with increasing Li-ion extraction from GeP electrode at high potential, as schematically illustrated in Fig. 6b. The healed local structure would further re-construct the initial layered crystal structure of GeP rather than degrade to a mixture of Ge and amorphous P via electrochemical aggregation. As a result, a small driving force like relative high charge potential can excite structural recovery of GeP. Meanwhile,

for FeP anode, the large formation energy means that Fe-P bonds are rather stable and very difficult to reform once converted by lithiation. The charge potential driving force is not sufficient to conquer energy barrier to re-construct Fe-P bonds and thus little initial bonding chemistry of FeP can be re-covered after Li-ion extraction. With increasing charge potential driving force, Fe domains would become larger and eventually form large aggregations, as presented in Fig. 6d. Note that self-healing-ability of all these crystal structure involve certain similarities: e.g., approaching atomic electronegativity, special layered structure and excellent transfer capability of the Li-ion and electron configurations.

3.6. The Li-storage performance enhancement of GeP/C composite

From above analysis on Li-storage performance and mechanism, we conclude that layered GeP is a promising anode material candidate with a special Li-storage mechanism while hindered by its limited cycle-life. As known, carbon composite is an effective way to promote cycle-life and rate performances, dramatically [26]. Herein, to enhance its cycle stability to a practical level, we further composited the lab-prepared GeP with low-cost commercial graphite by a facile second ball milling. As exhibited morphology by low-magnitude FSEM (Fig. S18a) and TEM images (Fig. 7a), the as-synthesized GeP/C composite was combined with each other densely. The high-magnitude FSEM image (Fig. S18b) exhibits the composite obtains refined micro-morphology and the halolike ring with dot-distributed SAED pattern (inset of Fig. 7a) further indicates the slightly reduced crystallization of GeP. As observed in the elemental mappings of GeP/C composite presented in Fig. 7b-c, three elements Ge, P and C are well-overlapped, similar to the scanning transmission electron microscope (STEM) image framework (Fig. 7b) of GeP/C composite, indicating that the layered GeP was highly composited with layered graphite. The highly composited electrode would strengthen the electrode integrity during repeated discharge/charge process to enhance cycle-life and endow faster transport of the Li-ion and electron. As expected, the life-span (Fig. 7d) of the composited GeP/C electrode can be substantially extended to 600 cycles with a reversible capacity over $1750\,\text{mA}\,\text{h}\,\text{g}^{-1}$ at a current density of $200\,\text{mA}\,\text{g}^{-1}.$ The cycle stability is the best among all reported Ge-based anodes at similar current density, as compared with other Ge-based anode summarized in Fig. 7f [2,3,27-51]. The initial coulombic efficiency of GeP/C electrode is also above 90%, and the second is up to 99.5%, comparable to that of commercial graphite, which indicates high reversibility of the electrode. Also, seen from the comparison with other Ge-based anodes shown in Fig. 7f, this value is also the best. Apart from superior reversibility, large capacity and long cycle-life, rate performance of GeP/C was also highly expected. As shown in Fig. 7e, with promoting current density from 0.1 to 0.2, 0.3, 0.5, 1, 2, 3 A g^{-1} , the reversible capacity can be retained at 1750 (100%, the capacity retention rate, compared with the initial reversible capacity), 1695 (97%), 1640 (94%), 1565 (89.4%), 1430 (82%), 1295 mA h g⁻¹ (74%), 1210 mA h g⁻¹ (69%), respectively. Even at an aggressive current density of 5 A g⁻¹ (50 times larger than initial current density), the reversible capacity can be still be maintained up to 63%. The ultra-high rate performance and ultra-long life span of GeP/C composite mainly benefit from the following factors. 1) The self-healing Li-storage mechanism not only regain initial structural advantages of GeP like fast transfer of the Li-ion and electron but also effectively mitigate electrode structural degradation. 2) the intercalation compound Li_xGeP achieves metallic conductivity and faster Li-ion transportation than that of Ge, and upon the following in-depth lithiation stage, the produced Li₃P can serve as the shielding matrix to alleviate aggregation issues and provide Li-ion transfer channel for further lithiation of Li_x Ge (x < 3.75). 3) The carbon matrix and reduced particle size of GeP could boost the electrolyte infiltration, shorten Li-ion diffusion length and accelerate reaction kinetics, thus improving rate performance.

4. Conclusion

In summary, a novel layered Ge-based GeP anode material and its carbon composite have been originally synthesized using a facile ball milling process followed by low-temperature annealing. When initiated as an anode material for LIBs, the layered GeP anode shows much better performance than Ge, due not only to faster transport of the Li-ion and electron but also to the interesting Li-storage mechanism that involves intercalation, conversion, and alloying reaction, as co-confirmed by XRD, TEM, XPS, Raman spectroscopy, and electrochemical measurements. The lavered crystal structure of GeP can be re-constructed during charging, thus regaining its structural advantages after each cycling, offering excellent reversibility. The GeP/C composite demonstrates the best performances among Ge-based anodes in terms of reversibility, cyclability and reaction kinetics. The special healing phenomenon was derived from low formation energy, according to firstprinciple calculations. It is believed that formation energy could be an important parameter for rational design of better anode materials for LIBs.

Acknowledgements

This work was supported by the National Natural Science Foundation of China (21701030, 51801096, 51702241), Guangdong Province Natural Science Foundation (2017A030310241), Innovative talents cultivation project of outstanding youth in Guangdong Province (2016KQNCX038), Science and Technology Planning Project of Guangzhou City (201804010392), China Postdoctoral Science Foundation funded project (No. 1112000139), Guangdong Innovative and Entrepreneurial Research Team Program, China (No. 2014ZT05N200), and US National Science Foundation (DMR-1742828). The authors acknowledge the use of facilities in Guangdong University of Technology, Georgia Institute of Technology, and Southern University of Science and Technology.

Appendix A. Supplementary data

Supplementary data to this article can be found online at https://doi.org/10.1016/j.nanoen.2019.04.080.

References

- [1] J.H. Kim, J.H. Yun, D.K. Kim, Adv. Energy Mater. 8 (2018) 1703499.
- [2] W. Xiao, J. Zhou, L. Yu, D. Wang, X.W. Lou, Angew. Chem. 55 (2016) 7427–7431.
- [3] D. Li, H. Wang, H.K. Liu, Z. Guo, Adv. Energy Mater. 6 (2016) 1501666.
- [4] J. Sun, G. Zheng, H. Lee, N. Liu, H. Wang, H. Yao, W. Yang, Y. Cui, Nano Lett. 14 (2014) 4573–4580.
- [5] S. Haghighat-Shishavan, M. Nazarian-Samani, M. Nazarian-Samani, H.K. Roh, K.Y. Chung, B.W. Cho, S.F. Kashani-Bozorg, K.B. Kim, J. Mater. Chem. A 6 (2018) 10121–10134
- [6] D. Sun, X. Zhu, B. Luo, Y. Zhang, Y. Tang, H. Wang, L. Wang, Adv. Energy Mater. 8 (2018) 1801197.
- [7] C. Wu, P. Kopold, P.A. van Aken, J. Maier, Y. Yu, Adv. Mater. 29 (2017) 1604015.
- [8] X. Xu, J. Liu, Z. Liu, Z. Wang, R. Hu, J. Liu, L. Ouyang, M. Zhu, Small 14 (2018) 1800793.
- [9] Y. Lu, P. Zhou, K. Lei, Q. Zhao, Z. Tao, J. Chen, Adv. Energy Mater. 7 (2017) 1601973.
- [10] J. Liu, S. Wang, K. Kravchyk, M. Ibáñez, F. Krumeich, R. Widmer, D. Nasiou, M. Meyns, J. Llorca, J. Arbiol, M.V. Kovalenko, A. Cabot, J. Mater. Chem. A 6 (2018) 10958–10966.
- [11] X. Fan, J. Mao, Y. Zhu, C. Luo, L. Suo, T. Gao, F. Han, Adv. Energy Mater. 5 (2015) 1500174.
- [12] Y. Xu, B. Peng, F.M. Mulder, Adv. Energy Mater. 8 (2018) 1701847.
- [13] W. Li, H. Li, Z. Lu, L. Gan, L. Ke, T. Zhai, H. Zhou, Energy Environ. Sci. 8 (2015) 3629–3636.
- [14] H.T. Kwon, C.K. Lee, K.J. Jeon, C.M. Park, ACS Nano 10 (2016) 5701-5709.
- [15] P.C. Donohue, H.S. Young, J. Solid State Chem. 1 (1970) 143–149.
- [16] C. Barreteau, B. Michon, C. Besnard, E. Giannini, J. Cryst. Growth 443 (2016) 75–80.
- [17] Y. Wei, L. Huang, J. He, Y. Guo, R. Qin, H. Li, T. Zhai, Adv. Energy Mater. 8 (2018) 1703635.
- [18] F. Li, Y. Qu, M. Zhao, J. Mater. Chem. A 4 (2016) 8905–8912.
- [19] W. Tian, S. Zhang, C. Huo, D. Zhu, Q. Li, L. Wang, X. Ren, L. Xie, S. Guo, P.K. Chu,

- H. Zeng, K. Huo, ACS Nano 12 (2018) 1887-1893.
- [20] K. Zhang, M. Park, L. Zhou, G.H. Lee, J. Shin, Z. Hu, S.L. Chou, J. Chen, Y.M. Kang, Angew. Chem. 55 (2016) 12822–12826.
- [21] Y. Fu, Q. Wei, G. Zhang, S. Sun, Adv. Energy Mater. 8 (2018) 1702849.
- [22] L.Y. Lim, S. Fan, H.H. Hng, M.F. Toney, Adv. Energy Mater. 5 (2015) 1500599.
- [23] D.T. Ngo, H.T.T. Le, C. Kim, J.Y. Lee, J.G. Fisher, I.D. Kim, C.J. Park, Energy Environ. Sci. 8 (2015) 3577–3588.
- [24] Z. Li, L. Zhang, X. Ge, C. Li, S. Dong, C. Wang, L. Yin, Nano Energy 32 (2017) 494–502.
- [25] W.J. Li, S.L. Chou, J.Z. Wang, H.K. Liu, S.X. Dou, Chem. Commun. 51 (2015) 3682–3685.
- [26] S.O. Kim, A. Manthiram, ACS Appl. Mater. Interfaces 9 (2017) 16221-16227.
- [27] R. Mo, D. Rooney, K. Sun, H.Y. Yang, Nat. Commun. 8 (2017) 13949.
- [28] H. Kim, Y. Son, C. Park, M.J. Lee, M. Hong, J. Kim, M. Lee, J. Cho, H.C. Choi, Nano Lett. 15 (2015) 4135–4142.
- [29] G.T. Kim, T. Kennedy, M. Brandon, H. Geaney, K.M. Ryan, S. Passerini, G.B. Appetecchi, ACS Nano 11 (2017) 5933–5943.
- [30] C.K. Chan, X.F. Zhang, Y. Cui, Nano Lett. 8 (2008) 307-309.
- [31] S. Liu, J. Feng, X. Bian, Y. Qian, J. Liu, H. Xu, Nano Energy 13 (2015) 651-657.
- [32] D. Li, H. Wang, T. Zhou, W. Zhang, H.K. Liu, Z. Guo, Adv. Energy Mater. 7 (2017) 1700488.
- [33] C. Kim, G. Hwang, J.W. Jung, S.H. Cho, J.Y. Cheong, S. Shin, S. Park, I.D. Kim, Adv. Funct. Mater. 27 (2017) 1605975.
- [34] Y. Sun, S. Jin, G. Yang, J. Wang, C. Wang, ACS Nano 9 (2015) 3479-3490.
- [35] X. Li, Z. Yang, Y. Fu, L. Qiao, D. Li, H. Yue, D. He, ACS Nano 9 (2015) 1858–1867.
- [36] W. Li, Y.X. Yin, S. Xin, W.G. Song, Y.G. Guo, Energy Environ. Sci. 5 (2012)

- [37] K.H. Seng, M.H. Park, Z.P. Guo, H.K. Liu, J. Cho, Angew. Chem. 51 (2012) 5657–5661.
- [38] X.L. Wang, W.Q. Han, H. Chen, J. Bai, T.A. Tyson, X.Q. Yu, X.J. Wang, X.Q. Yang, J. Am. Chem. Soc. 133 (2011) 20692–20695.
- [39] D. Xue, S. Xin, Y. Yan, K. Jiang, Y. Yin, Y. Guo, L. Wan, J. Am. Chem. Soc. 134 (2012) 2512–2515.
- [40] X. Wang, L. Fan, D. Gong, J. Zhu, Q. Zhang, B. Lu, Adv. Funct. Mater. 26 (2016) 1104–1111.
- [41] F.W. Yuan, H.J. Yang, H.Y. Tuan, ACS Nano 6 (2012) 9932–9942.
- [42] Y. Yu, C. Yan, L. Gu, X. Lang, K. Tang, L. Zhang, Y. Hou, Z. Wang, M.W. Chen, O.G. Schmidt, J. Maier, Adv. Energy Mater. 3 (2013) 281–285.
- [43] J. Gu, S.M. Collins, A.I. Carim, X. Hao, B.M. Bartlett, S. Maldonado, Nano Lett. 12 (2012) 4617–4623.
- [44] H. Kim, Y. Son, C. Park, J. Cho, H.C. Choi, Angew. Chem. 52 (2013) 5997-6001.
- [45] J. Liu, K. Song, C. Zhu, C.C. Chen, P.A. Van Aken, J. Maier, Y. Yu, ACS Nano 8 (2014) 7051–7059.
- [46] C. Yan, W. Xi, W. Si, J. Deng, O.G. Schmidt, Adv. Mater. 25 (2013) 539-544.
- [47] M.H. Park, Y. Cho, K. Kim, J. Kim, M. Liu, J. Cho, Angew. Chem. 50 (2011) 9647–9650.
- [48] T. Song, H. Cheng, H. Choi, J. Lee, H. Han, D.H. Lee, D.S. Yoo, M. Kwon, J. Choi, S.G. Doo, H. Chang, J. Xiao, ACS Nano 6 (2012) 303–309.
- [49] M.H. Seo, M. Park, K.T. Lee, K. Kim, J. Kim, J. Cho, Energy Environ. Sci. 4 (2011)
- [50] R. Yi, J. Feng, D. Lv, M.L. Gordin, S. Chen, D. Choi, D. Wang, Nano Energy 2 (2013) 498–504.
- [51] Y. Chen, C. Yan, O.G. Schmidt, Adv. Energy Mater. 3 (2013) 1269-1274.